Viscophoretic particle transport

Vahid Khandan,[1] Vincent Boerkamp,[2] Abbas Jabermoradi,[2] Mattia Fontana,[2]
Johannes Hohlbein,[2,3] Elisabeth Verpoorte,[1] Ryan C. Chiechi,[4] and Klaus Mathwig[1,5,*]

[1]*University of Groningen, Groningen Research Institute of Pharmacy,*
Pharmaceutical Analysis, P.O. Box 196, XB20, 9700 AD Groningen, The Netherlands
[2]*Laboratory of Biophysics, Wageningen University and Research,*
Stippeneng 4, 6708 WE Wageningen, the Netherlands
[3]*Microspectroscopy Research Facility, Wageningen University and Research,*
Stippeneng 4, 6708 WE Wageningen, The Netherlands
[4]*Department of Chemistry & Organic and Carbon Electronics Laboratory,*
North Carolina State University, Raleigh, NC, 27695 USA
[5]*imec within OnePlanet Research Center, Bronland 10, 6708 WH Wageningen, The Netherlands*
(Dated: December 23, 2022)

Viscosity is a fundamental property of liquids. It determines transport and diffusion of particles in solution. Nonetheless, it is an open question how a *gradient* of viscosity—causing a gradient in diffusivity—can lead to *viscophoretic transport*, i.e., directed transport of particles and molecules in solution. Here, we determine viscophoretic drift experimentally. We generate steep, stable viscosity gradients in a microfluidic device and image transport of suspended nanoparticles in these gradients using high-resolution microscopy. We observe high viscophoretic drift velocities which significantly exceed theoretical predictions. In addition, we demonstrate a new method for trapping and concentrating particles by using the interplay of *viscophoresis* and *diffusiophoresis*. We believe that a quantification of viscophoresis will advance the understanding and application of transport processes of gradients of viscosity occurring in very diverse fields such as cell biology, chromatography, and membrane technology.

Introduction

Viscosity is an important property of liquids; it determines transport and diffusion of solvent particles, molecules and ions. A *gradient* in viscosity generates a gradient in the diffusion coefficient. This gradient leads to a molecular transport phenomenon: viscophoresis. Although viscosity gradients play an important role in various natural and artificial systems, it is not understood how transport of particles and molecules is driven by such a gradient. This lack of knowledge is a major research gap.

Transport phenomena of particles and molecules in solution due to gravity, electrical fields and concentration gradients have been studied in great detail and are well understood. In stark contrast, the transport of particles in a gradient of viscosity has never been investigated systematically at the single-particle level.

Understanding transport effects based on viscosity gradients is important because they exist in nature such as microviscosity of cellular organelles [1]; and a new 'phoretic' phenomenon can be exploited in engineering applications, e.g., for sensing and manipulation of molecules and particles. In a broader sense, researching fluidic viscosity gradients could be of importance in very different scientific fields in viscosity gradients on larger length scales, such as magma viscosity gradients in volcanoes [2], gradients in planets [3], or stellar plasma [4].

Here, we experimentally answer the fundamental question: How is the motion of a particle or molecule in solution affected by a gradient in viscosity? Viscophoretic drift has been inferred from measurements of electrical conductivity [5], but it it has never been observed directly at the single-particle level.

The concept of viscophoretic transport is shown in Figure 1. A particle or molecule in solution undergoes a diffusive Brownian walk in a gradient of viscosity. As viscosity decreases from left to right, the diffusivity of the particle increases. Brownian steps toward the right (higher diffusivity) are larger than toward the left (higher viscosity). Therefore, the particle experiences a net drift towards the right side in the direction of lower viscosity and higher diffusivity [5].

We combine novel microfluidic devices which allow us to generate very steep, stable viscosity gradients and high-resolution fluorescence imaging and correlation analysis. This experimental setup enables to determine drift *directly* at the single-particle level and, thus, to
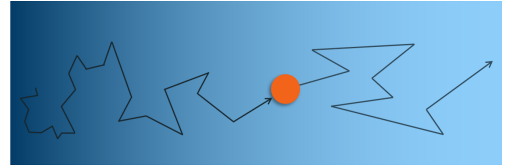

FIG. 1. Schematic of *viscophoretic* transport: A particle is driven from viscous to a low-viscosity fluid from left to right. Its diffusion coefficient in this direction increases, and steps of the Brownian walk become longer—leading to net transport toward lower viscosity.

* klaus.mathwig@imec.nl

demonstrate viscophoresis. Quantitatively, we find that viscophoretic drift velocities are much larger than predicted, in particular for larger nanoparticles. In addition to determining drift velocities, we find a new microfluidic principle for trapping and concentrating nanoparticles by making use of the combination of viscophoresis and diffusiophoresis.

Theory and state of the art

A gradient in viscosity leads to a gradient in diffusivity. Determining drift caused by such a gradient boils down to answering the question: How can Fick's law

$$\boldsymbol{J} = -\boldsymbol{D}\frac{\partial c(x)}{\partial x} \tag{1}$$

be generalized for a space-dependent diffusivity $\boldsymbol{D} = \boldsymbol{D}(x)$ ($\boldsymbol{J}$: diffusive flux, c: analyte concentration)? Here, transport is a phenomenon with multiplicative feedback, i.e., the Brownian diffusion exhibits a state-dependent noise intensity [6], and transport *cannot* be derived from first principles. This ambiguity for evaluating trajectories in nonuniform stochastic noise is called the *Itô-Stratonovich dilemma* [7, 8]. Possible solutions of the noise-induced viscophoretic drift velocity v_{VP} of a particle include

$$v_{\mathrm{VP}} = \langle \dot{x} \rangle = \alpha \frac{\mathrm{d}D(x)}{\mathrm{d}x} \text{ with } \alpha = \{0, \tfrac{1}{2}, 1\}, \tag{2}$$

with the Itô ($\alpha = 0$, no viscophoresis), Stratonovich ($\alpha = \frac{1}{2}$), and isothermal ($\alpha = 1$) choice.[1]

For colloidal particles generally the isothermal process is considered by theory, i.e., fast drift with $\alpha = 1$ is chosen [10, 11].

State-of-the-art research in transport driven by steady-state viscosity gradients has been performed by Wiener and Stein [5]. Using an H-shaped microchannel geometry and driving flow of carrying solutions with different viscosities, the steady-state non-equilibrium condition of a stable viscosity gradient is established in a 'mixing channel' while suppressing any net mass transport (i.e., flow). A viscophoretic drift of ions with $\alpha = 1$ was inferred by an electrical ensemble measurement sensing the ion current through the mixing channel.

Experimental concept

Our experimental setup is shown in Figure 2. Using a microfluidic H-channel device in glass and polydimethyl-

---

[1] From the point of view of a Brownian walker, for $\alpha = 0$ the step length of the walk depends on the diffusivity at the starting position (Itô process, no viscophoresis), for $\alpha = 1$ on the diffusivity at the end point of the step (isothermal process), and for $\alpha = \frac{1}{2}$ the midpoint diffusivity (Stratonovich process) [5, 9].
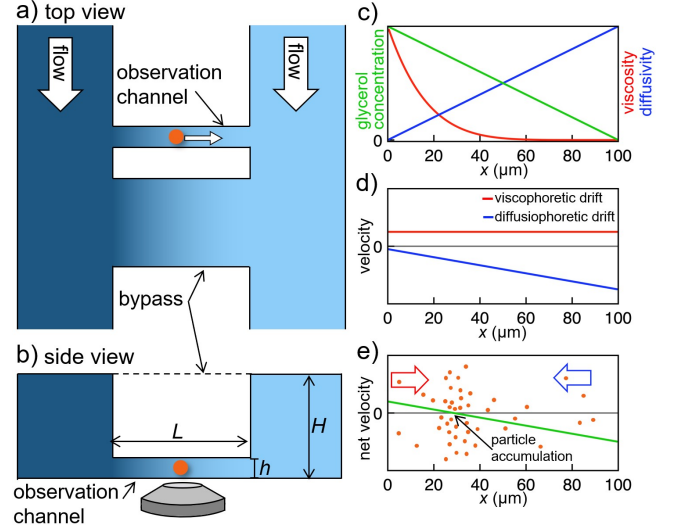

FIG. 2. a) Top view and b) side view of schematic of microfluidic experimental setup. A stable viscosity gradient (blue color gradient) is generated in the $2\,\mu\mathrm{m}$ shallow observation channel with suppressed flow using a downstream bypass ($L = 100\,\mu\mathrm{m}$, $h = 2\,\mu\mathrm{m}$, $H = 200\,\mu\mathrm{m}$). c) Gradient of glycerol concentration (green curve) and resulting gradients of viscosity (red) and diffusivity (blue) in the observation channel. d) Resulting viscophoretic and diffusiophoretic drift velocities of suspended nanoparticles, and e) resulting overall net velocity leading to particle accumulation in a channel segment.

siloxane, two syringe pumps deliver flow of aqueous solutions with different glycerol concentrations, and, thus, different viscosities [12]. Flow rates are adjusted to prevent any pressure-driven flow and any solvent mass transport in the observation channel. Thus, the steep, stable viscosity gradient is generated there. By using a narrow observation microchannel with a large hydraulic resistance, and a wide pressure-releasing bypass channel positioned directly downstream, any residual flow in the observation channel is suppressed efficiently. Fluorescent nanoparticles are suspended in both inlet solutions, any particle adsorption on channel surfaces is prevented by chemical surface modification. Nanoparticle drift is mapped in the observation channel by fluorescent imaging and image correlation analysis.

Figure 2c-e shows gradients in the observation channel. The glycerol concentration decreases linearly from left to right, resulting in a viscosity decreasing with $\eta \propto 1/x$ and a linearly increasing nanoparticle diffusivity D [5]. Thus, according to eq. (2), a constant positive drift velocity from left to right is expected.

Colloidal particles suspended in a chemical gradient undergo diffusiophoresis [13]. For a nonelectrolyte concentration gradient, particles drift with a diffusiophoretic velocity $v_{\mathrm{DP}} \propto \frac{1}{\eta(x)}\mathrm{d}c_{\mathrm{gly}}/\mathrm{d}x$ [14–17]. Here, glycerol molecules are diffusing around polystyrene particles, causing drift toward a higher glycerol concentration. The velocity v_{DP} increases linearly from left to right.

Video 1. 110-nm polystyrene nanoparticles undergoing viscophoretic and diffusiophoretic drift in opposing direction leading to accumulating in a segment of a $150\,\mu$m long microchannel the channel. Video is sped up 6 times. Dashed lines indicate microchannel walls.

Serendipitously, diffusiophoretic drift and expected viscophoretic drift have opposite directions, and, thus, the effects can be distinguished directly. The resulting net particle velocity (see Fig. 2e) decreases linearly along the observation channel starting with a positive velocity dominated by viscophoresis on the left side, crossing over to a negative net velocity (i.e., transport from right to left) dominated by diffusiophoresis on the right channel side. In effect, particles move from both sides toward a point at which $v_{\mathrm{net}} = v_{\mathrm{VP}} - v_{\mathrm{DP}} = 0\,\mu$m/s, and they accumulate there.

Experimental viscophoresis

Video 1 shows fluorescent particles with a $110\,$nm diameter accumulating in the observation microchannel. Particles are entering the channel by diffusion from the left and right inlet channels. Within the glycerol viscosity gradient they are transported from left to right due to viscophoresis, and driven from right to left by diffusiophoresis—leading to accumulation on a left-side segment of the microchannel. Diffusiophoresis is the dominant transport mechanism along most of the channel, it vanishes though toward the left side, where transport toward the channel center is entirely viscophoretic.

Experimental results demonstrating viscophoresis of particles with a diameter of $28\,$nm are shown in Figure 3. As particles undergo viscophoresis and diffusiophoresis they continue accumulating in a segment of the microchannel centered at $v_{\mathrm{net}} = 0\,\mu$m/s positioned around $x = 25\,\mu$m. In Figure 3b fluorescent intensity profiles are depicted of particles accumulation over 2.5 min. Intensity profiles exhibit a Poisson shape expected for diffusive broadening of the accumulation zone.

Fluorescence imaging with high spatial and temporal resolution enables us to use correlation analysis of video frames to *map* magnitude as well as direction of nanoparticle drift and diffusion in the observation channel. Figure 3c shows a map of the time-average *direction* (arrows) of particle drift and its *magnitude* in longitudinal direction (x-direction along channel, color map). The overall mean drift v_{net} can directly be extracted from this data by averaging over the y-direction across the channel. The resulting net drift velocity $v_{x,\mathrm{net}}$ is shown in Figure 3d. Here, the light green curve depicts the confidence interval obtained via three separate measurements;
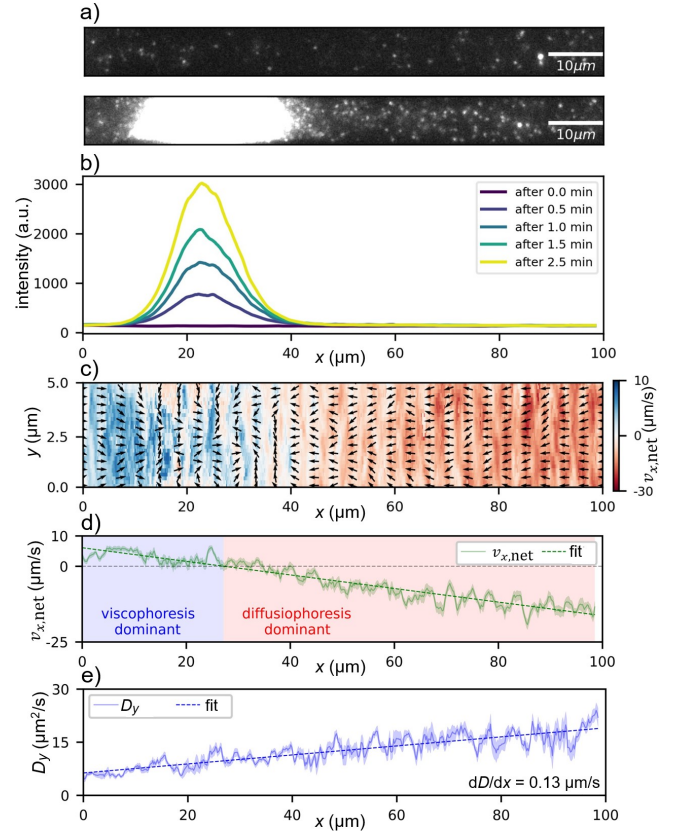

FIG. 3. Experimental results of observing viscophoretic drift by imaging 28-nm particles in a viscosity gradient defined by an aqueous solution with glycerol content ranging from 50% on the left site to 0% on the right. a) Still images and b) fluorescence intensity graph of particles drifting due to viscophoresis and diffusiophoresis and accumulating over time in a left-hand side segment of a microfluidic channel. c) Map of experimental drift velocity in a microchannel determined via image correlation. d) Average drift velocity $v_{x,\mathrm{net}}$ along the channel in x-direction extracted from panel c. e) Average diffusion coefficient along the channel (diffusivities are evaluated in vertical y-direction). Light green and light blue curve denoted confidence intervals; fits are linear.

the dashed line is a linear fit. Data in Figure 3a-d clearly show two distinct transport regimes of particle transport in opposite directions dominated by viscophoresis and diffusiophoresis, respectively. In the far left channel segment, in which diffusiophoresis is vanishing, viscophoresis is observed and clearly distinct from diffusive noise. We determine a viscophoretic drift velocity of $7\,\mu$m/s.

By using image correlation analysis to determine the mean square displacement of particles in y-direction (in which no drift occurs), we determine particle diffusivities in a measurement that is entirely unaffected by longitudinal drift. The resulting coefficient D is shown in Figure 3e. This linear diffusivity profile is in agreement with expectations (blue curve in Figure 2c), clearly confirming a stable gradient without any observable nonlinear distortion that would be caused by residual flow.

Excluding interfering transport effects

The main result of the present work is the direct observation of viscophoresis as a new transport effect. Therefore, it is necessary to carefully control or eliminate any other transport mechanism which could provide an alternative explanation for this observed transport. The most obvious candidate for parasitic transport is *flow*, i.e., net mass transport of the solvent that is exerting Stokes forces on analyte particles. We suppress and rule out residual flow in the observation channel in several ways:

(1) Applied inflow rates are set equal to the inverse of the viscosity ratios to minimize the generation of a pressure difference between inlet channels. In the microfluidic design, the inlet channels have a wide cross section while the observation channel is very shallow—leading of a ratio of the respective hydraulic resistances [18] of approximately 1:10.000.000. Consequently, even a large parasitic difference in inlet flow rates of 10% will lead to a residual flow velocity of at most 30 nm/s in the observation channel, which is negligible compared to particle diffusion at the timescale of image acquisition ($> 3\,\mu$m in 10 ms) as well as compared to observed drift velocities.

(2) In a new microfluidic design, we use a *bypass* channel with a large cross section positioned directly downstream of the observation channel (see Fig. 2a,b). Any residual pressure difference between both ends of the observation channel is released via this bypass. Observation of a meniscus of side-by-side flow of high-glycerol and no-glycerol solvent in this bypass (data not shown) is further evidence of a negligible pressure difference between and negligible cross flow between both inlet channel.

(3) Pressure-driven flow would lead to a parabolic profile of Hagen-Poiseuille flow in the channel [18]. However, the mapped particle velocity (see Fig. 3c) shows a constant profile in y-direction of the cross section in agreement with visco-/diffusiophoretic transport as further proof that flow is absent in the observation channel.

Electrokinetic effects such as electrophoresis do not occur as no electric potential is applied anywhere in the setup. A constant concentration of background electrolyte (10 mM NaOH) suppresses electrostatic particle-wall interactions. Particle adsorption on the channel wall is further prevented by surface modification.

Only *diffusiophoretic* motion cannot be suppressed as it is a direct consequence of the glycerol concentration gradient. Nonetheless, as shown above, diffusiophoretic transport is directly distinguished from viscophoresis due its opposite direction—and the superposition of both effects leads to a new principle of particle accumulation in the observation channel.

Quantifying viscophoresis

To determine the magnitude of viscophoretic drift and its dependency on the viscosity gradient and particle size, we varied this gradient by changing glycerol concentrations, and we observed drift of three types of particles with diameters of 110 nm, 28 nm (both polystyrene), and 8 nm (CdTe quantum dots), respectively. The viscophoretic drift magnitude was determined by evaluating a linear fit of experimental drift $v_{x,\text{net}}$ at the position of the far-left channel entrance (position of negligible diffusiophoresis), i.e., $v_{\text{VP}} = v_{x,\text{net}}(x = 0\,\mu\text{m})$. Experimental results are shown in Figure 4 and reveal several characteristics:

The magnitude of viscophoresis increases with the viscosity gradient (see Fig. 4b).

Surprisingly, a clear dependence of viscophoretic drift velocity on particle size is not observed within the accuracy of our measurement. We sense fasted drift for the intermediate 28 nm particle size.

Measured diffusivity profiles $D(x)$ and gradients $\mathrm{d}D(x)/\mathrm{d}x$ (data not shown) are in good agreement with diffusivities expected for hydrodynamic particle diameters of the polystyrene nanoparticles, with smaller particles diffusing faster (see Fig. 4c). 8-nm CdTe quantum dots diffuse quickly however, their measured diffusivity corresponds to a hydrodynamic diameter of approximately only 4 nm.

In Figure 4d, the parameter $\alpha = v_{\text{VP}}/(\mathrm{d}D/\mathrm{d}x)$, compare eq. (2), is plotted for the different particle sizes, ranging from $\alpha = 12$ for 8-nm particles to $\alpha = 95$ and $\alpha = 140$ for 28-nm and 110-nm particle, respectively. α clearly increases with particle size. This observation is unexpected. Theory [10, 11] as well as experimental results on viscophoresis of ions [5] report on an *isothermal* transport regime with a viscophoretic drift velocity that is proportional to $\mathrm{d}D/\mathrm{d}x$. I.e., v_{VP} is expected to scale *inversely proportional* with the particle diameter, and $\alpha = 1$ is expected to be constant. In contrast, we observe that α is varying and that α and consequently, viscophoretic drift is much larger and faster than expected. In other words, while viscophoresis is expected to vanish with increase particle size, we observe that larger nanoparticles are drifting as fast as small quantum dots. Equation (2) with a constant α is not suited well to describe our observation.

The expectation of smaller viscophoresis for larger particles makes sense intuitively because viscophoresis is driven by diffusion, and the diffusion coefficient decreases with increasing particle size. We speculate why we do *not* observe this decrease. While larger particles diffuse slower, their larger diameter samples a wider segment of the gradient of viscosity and diffusivity, respectively. This means, the difference of diffusivity experienced at both ends of a particle increases linearly with the particle's diameter, speculatively leading to stronger viscophoretic drift. This effect approximately cancels out the reduced diffusivity due to larger size. For small analytes with a size comparable to the viscosity-inducing glycerol molecules, viscophoresis is then governed by eq. (2) with $\alpha = 1$ in agreement with the state of the art.
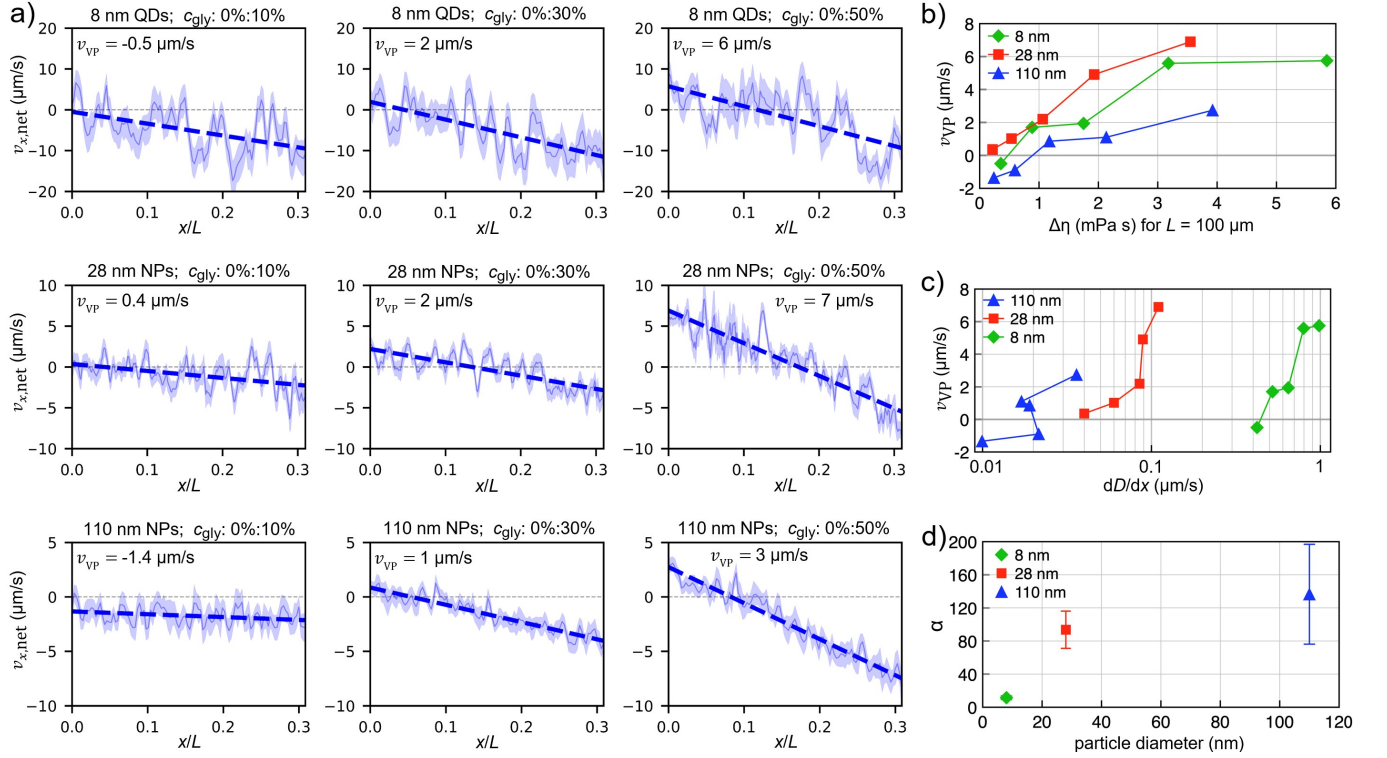
FIG. 4. a) Drift velocities $v_{x,\text{net}}$ as a function of particle size and viscosity gradient. Velocity profiles for particles with diameters of 8 nm, 28 nm, and 110 nm (rows) are shown. Viscosity gradients were adjusted by adding glycerol with weight percentage 10%, 30%, 50% in the left-side inlet solution (columns). $v_{x,\text{net}}$ are determined by averaging mapped velocities in y-direction. Data and confidence intervals on the left 30% of microchannels is show; fits are linear. b) Viscophoretic drift velocities obtained as $v_{\text{VP}} = v_{x,\text{net}}(x = 0\,\mu\text{m})$ as a function of viscosity difference $\Delta\eta$ of 0% glycerol weight content (right inlet) vs. 10%, 20%, 30%, 40%, 50% (left inlet). $\Delta\eta$ is normalized to a $100\,\mu\text{m}$ channel length as different devices were used (effectively $L = 85\,\mu\text{m}$ for 8 nm, $L = 141\,\mu\text{m}$ for 28 nm, and $L = 127\,\mu\text{m}$ for 110 nm particles). c) Linear-log plot of v_{VP} as function of the particle diffusivity gradient $\mathrm{d}D/\mathrm{d}x$. Here $\mathrm{d}D/\mathrm{d}x$ was determined experimentally as shown Fig. 3e. d) α parameter obtained as slope of a linear fit to curves in panel c, i.e., $v_{\text{VP}} = \alpha\,\mathrm{d}D/\mathrm{d}x$. Error bars show standard error of linear regression. Lines in b, c are guides for the eye.

Conclusions

We have demonstrated viscophoretic transport in steep microfluidic viscosity gradients and directly imaged viscophoretic particle drift for the first time using fluorescence microscopy. Experimental results show fast drift of nanoparticles with velocities that do *not* decrease with increasing particle size and are significantly larger than expected for an isothermal transport regime.

Understanding viscophoresis quantitatively has potentially a high impact in various fields such as in molecular trans-membrane transport in organelles of different microviscosities [1]. Controlling viscophoretic transport could be utilized, for example to increase separation performance when injecting a viscous carrier liquid in a chromatography column. In nanopore sensing, viscophoresis could be employed to control and slow analyte translocation times [19].

In addition to viscosity-driven transport, we have demonstrated a new principle for accumulation of particles using the interplay of viscophoretic and diffusiophoretic drift. Upconcentrating or (reversible) trapping of molecules using opposing viscophoresis and diffusiophoresis could add to the biophysical toolkit [20] as a method for manipulating molecules.

Appendix A: Materials

Water in all used samples was purified using a MilliQ system (Millipore, Billerica, MA, USA). Carboxylated polystyrene nanoparticles with 660 nm/680 nm and 505 nm/515 nm excitation/emission wavelength and average diameter of 28 nm and 110 nm, respectively, were purchased from Thermofisher scientific (Eugene, Oregon, USA), catalog numbers F8803 and F8783. Car-

boxylated CdTe quantum dots with a nominal diameters of 8.6 nm and 780 nm emission wavelength and excitation wavelength below 400 nm were purchased from PlasmaChem GmbH (Berlin, Germany). Succinic anhydride, (3-aminopropyl)triethoxysilane (APTES), absolute ethanol, and dimethylformamide (DMF) were purchased from Sigma-Aldrich (The Netherlands). Sylgard 184 polydimethylsiloxane (PDMS) was purchased from Dow Corning (USA) and SU8 photoresist from MicroChem (Newton, MA, USA).

Aqueous solutions with glycerol concentrations ranging from 0% to 50% (w:w%) were prepared directly before the measurements. 10 mM NaOH was added as background electrolyte. After adding fluorescent particles, solutions were vortexed for 2 min.

Appendix B: Device fabrication, microfluidics, and surface modification

Stepwise parallel fabrication consisting of photolithography, soft lithography, and bonding was employed to fabricate microfluidic devices. First, a master mold was fabricated using photolithography in two layers of $2\,\mu m$ and $200\,\mu m$ of SU8-2002 and SU8-2100 negative photoresists, respectively, using spin-coating on 10-cm silicon wafer substrates, soft-baking, UV exposure, development, and post baking steps [21–23]. Afterwards, the structure was transferred from the fabricated master mold into PDMS to form microchannels. In this step, the ratio of PDMS elastomer to curing agent was kept at 10:1 (w:w) to obtain a high Young's modulus [24]; the curing process was carried out at 70°C for 2 h on a leveled hotplate. The molded PDMS compartments were subsequently bonded to borosilicate coverslips with $170\,\mu m$ thickness ($24\,mm \times 60\,mm$, Engelbrecht) following surface activation with oxygen plasma in a Harrick plasma cleaner at 42 kPa for 30 s.

The microfluidic device has two inlets channels (and an outlet) which are $200\,\mu m$ high, and an array of microchannels with a $2\,\mu m \times 5\,\mu m$ cross section and different nominal lengths ranging from $100\,\mu m$ to $150\,\mu m$ in different device designs. A microchannel array connects both inlet channels. The bypass channel positioned downstream of this array has a $200\,\mu m \times 500\,\mu m$ cross section and the same length as the channel in the array. A residual pressure difference between both inlets is released via the bypass. Inlet channels are connected to two $500\,\mu m$ glass syringes (ILS GmbH, Germany) via Tygon tubing with 0.25 mm/0.76 mm inner/outer diameter (Avantor VWR, USA). Syringes are filled with liquids of different viscosities; and flow is driven by two Harvard Apparatus 11 Pico Plus syringe pumps set to constant pump rates to generate a stable viscosity gradient along the observation channels. In order to eliminate residual flow in the observation channel, inflow rates were set equal to the inverse of the viscosity ratios during viscophoresis experiments. Mirofluidic inlet channels in

the device connect to a single outlet microchannel downstream of the microchannel array and bypass. This outlet is connected to a reservoir open to atmospheric pressure via PTFE tubing with 0.4 mm/0.8 mm inner/outer diameter—sufficiently wide to easily remove air bubbles trapped in the device.

The hydrophobic surface of PDMS and glass coverslips was modified to prevent the deposition of carboxylated fluorescent particles inside the microfluidic device. We adopted a strategy to functionalize interior surfaces with stable carboxyl groups which deprotonate at pH 12 (10 mM NaOH base), thus generating negatively charged surfaces for electrostatic repulsion of particles from the microchannel walls [25–27]. Surface modification followed three successive steps: 1) activation using oxygen plasma (30 s) to generate hydroxyl groups on the surfaces, 2) introducing 5% (v:v) (3-aminopropyl)triethoxysilane in absolute ethanol via the syringe pump at atmospheric pressure for 1 h at 70°C to passivate amine linkers, and 3) introducing 20 mM succinic anhydride in DMF at atmospheric pressure for 2 h at 100°C to generate carboxyl groups. Then, the treated devices were filled with deionized water and stored at room temperature until experimentation.

Appendix C: Microscopy and image analysis

Fluorescent microscopy was conducted using a home-build setup, openFrame [28]. The setup consists of a multimode laser unit with 402 nm, 520 nm, and 680 nm wavelengths (MatchBox, Integrated Optics, Lithuania) operating at 200 mW, 140 mW and 360 mW, respectively. The laser output was coupled into a $150\,\mu m \times 150\,\mu m$ square silica core, which promotes mode mixing in the fiber in order to obtain a uniform spatial distribution and a square beam shape compared to a Gaussian profile from a single mode fiber for the excitation beam (Thorlabs M102L05). An oil immersion objective (Apo TIRF 60x 1.49 NA, Nikon), a double band emission filter (ZET 532/640m-TRF), and a camera (Prime 95B sCMOS, 202, Photometrics) were implemented. The setup is controlled by the micromanager 1.4 software package, while the frame time is externally controlled in accordance with the laser pulses using a home build program, SMILE [29]. Effective pixel sizes of 180 nm and 360 nm result from 1 x 1 and 2 x 2 binning. Camera images are cropped into the microchannels before data acquisition to reach high acquisition rates of 200 fps and 500 fps, respectively.

Diffusometry and velocimetry were conducted based on the pair Correlation Function (pCF) [30, 31] and particle Image Velocimetry (PIV) [32] techniques. Image stacks of 68k frames were used to calculate pCF for each pixel relative to 25 neighboring pixels (for 8 nm and 28 nm particles) and 15 neighboring pixels (for 110 nm particles) neighboring pixels using Fast Fourier Transform for multiple lag times equivalent to 1 up to 12 frames. Then, eight coupled 1D Gaussian distributions were fitted into

each calculated pCF at each lag time to quantify the center's position and Mean Square Displacement (MSD) in eight directions sectioning a 2D surface of 360° into eight angular sectors of 90°, with 45°, overlap between two successive sectors. Afterwards, the drift velocity was calculated using a displacement taken at the center of the pCF. The diffusion coefficient in each direction was calculated using the time evolution of the quantified MSD.

---

[1] J. E. Chambers, M. Kubánková, R. G. Huber, I. López-Duarte, E. Avezov, P. J. Bond, S. J. Marciniak, and M. K. Kuimova, An Optical Technique for Mapping Microviscosity Dynamics in Cellular Organelles, ACS Nano **12**, 4398 (2018).

[2] T. Yamasaki and G. A. Houseman, The crustal viscosity gradient measured from post-seismic deformation: A case study of the 1997 Manyi (Tibet) earthquake, Earth and Planetary Science Letters **351-352**, 105 (2012).

[3] A. Morison, S. Labrosse, and G. Choblet, Sublimation-driven convection in Sputnik Planitia on Pluto, Nature **600**, 419 (2021).

[4] B. Bitsch, A. Morbidelli, E. Lega, K. Kretke, and A. Crida, Stellar irradiated discs and implications on migration of embedded planets: III. Viscosity transitions, Astronomy and Astrophysics **570**, 10.1051/0004-6361/201424015 (2014), arXiv:1408.1016.

[5] B. Wiener and D. Stein, Electrokinetic current driven by a viscosity gradient (2018), arXiv:1807.09106.

[6] G. Pesce, A. McDaniel, S. Hottovy, J. Wehr, and G. Volpe, Stratonovich-to-Itô transition in noisy systems with multiplicative feedback, Nature Communications **4**, 1 (2013).

[7] R. Mannella and P. V. E. McCintock, Itô versus Stratonovich: 30 Years Later, Fluctuation and Noise Letters **11**, 1240010 (2012).

[8] T. Kuroiwa and K. Miyazaki, Brownian motion with multiplicative noises revisited, Journal of Physics A: Mathematical and Theoretical **47**, 10.1088/1751-8113/47/1/012001 (2014), arXiv:1309.4189.

[9] O. Farago and N. Grønbech-Jensen, Langevin dynamics in inhomogeneous media: Re-examining the Itô-Stratonovich dilemma, Physical Review E - Statistical, Nonlinear, and Soft Matter Physics **89**, 1 (2014), arXiv:1305.6623.

[10] M. Yang and M. Ripoll, Brownian motion in inhomogeneous suspensions, Physical Review E - Statistical, Nonlinear, and Soft Matter Physics **87**, 1 (2013).

[11] A. Alizadeh, H. Daiguji, and A. M. Benneker, A theoretical understanding of ionic current through a nanochannel driven by a viscosity gradient, arXiv 10.48550/arXiv.2111.00054 (2021), arXiv:2111.00548.

[12] N. E. Dorset, *Properties of Ordinary Water Substances* (Reinhold Publishing, New York, 1940).

[13] B. Abécassis, C. Cottin-Bizonne, C. Ybert, A. Ajdari, and L. Bocquet, Boosting migration of large particles by solute contrasts, Nature Materials **7**, 785 (2008).

[14] J. L. Anderson, M. E. Lowell, and D. C. Prieve, Motion of a particle generated by chemical gradients Part 1. Non-electrolytes, Journal of Fluid Mechanics **117**, 107 (1982).

[15] P. O. Staffeld and J. A. Quinn, Diffusion-induced banding of colloid particles via diffusiophoresis, Journal of Colloid and Interface Science **130**, 69 (1989).

[16] J. S. Paustian, C. D. Angulo, R. Nery-Azevedo, N. Shi, A. I. Abdel-Fattah, and T. M. Squires, Direct Measurements of Colloidal Solvophoresis under Imposed Solvent and Solute Gradients, Langmuir **31**, 4402 (2015).

[17] S. Marbach, H. Yoshida, and L. Bocquet, Local and global force balance for diffusiophoretic transport, Journal of Fluid Mechanics **892**, A6 (2020).

[18] H. Bruus, Acoustofluidics 1: Governing equations in microfluidics, Lab on a Chip **11**, 3742 (2011).

[19] Y. Qiu, Z. S. Siwy, and M. Wanunu, Abnormal Ionic-Current Rectification Caused by Reversed Electroosmotic Flow under Viscosity Gradients across Thin Nanopores, Analytical Chemistry **91**, 996 (2019), arXiv:1811.12878.

[20] N. G. Walter, C.-Y. Huang, A. J. Manzo, and M. A. Sobhy, Do-it-yourself guide: how to use the modern single-molecule toolkit, Nature Methods **5**, 475 (2008).

[21] A. Mata, A. J. Fleischman, and S. Roy, Fabrication of multi-layer SU-8 microstructures, Journal of Micromechanics and Microengineering **16**, 276 (2006).

[22] A. del Campo and C. Greiner, SU-8: a photoresist for high-aspect-ratio and 3D submicron lithography, Journal of Micromechanics and Microengineering **17**, R81 (2007).

[23] T. A. Anhøj, *Fabrication of High Aspect Ratio SU-8 Structures for Integrated Spectrometers*, Ph.D. thesis, Technical University of Denmark (2007).

[24] A. Gokaltun, M. L. Yarmush, A. Asatekin, and O. B. Usta, Recent advances in nonbiofouling PDMS surface modification strategies applicable to microfluidic technology, TECHNOLOGY **05**, 1 (2017).

[25] S. Kralj, M. Drofenik, and D. Makovec, Controlled surface functionalization of silica-coated magnetic nanoparticles with terminal amino and carboxyl groups, Journal of Nanoparticle Research **13**, 2829 (2011).

[26] B. M. Cash, L. Wang, and B. C. Benicewicz, The preparation and characterization of carboxylic acid-coated silica nanoparticles, Journal of Polymer Science Part A: Polymer Chemistry **50**, 2533 (2012).

[27] Y. An, M. Chen, Q. Xue, and W. Liu, Preparation and self-assembly of carboxylic acid-functionalized silica, Journal of Colloid and Interface Science **311**, 507 (2007).

[28] openFrame: an open source approach to fluorescence microscopy, https://www.imperial.ac.uk/photonics/research/biophotonics/instruments--software/fluorescence-microscopy/openframe/, accessed: 2022-11-16.

[29] SMILE: Single Molecule Imaging Laser Engine, https://hohlbeinlab.github.io/miCube/LaserTrack_Arduino.html, accessed: 2022-11-16.

[30] C. Di Rienzo, F. Cardarelli, M. Di Luca, F. Beltram, and E. Gratton, Diffusion Tensor Analysis by Two-Dimensional Pair Correlation of Fluorescence Fluctuations in Cells, Biophysical Journal **111**, 841 (2016).

[31] C. Di Rienzo, E. Gratton, F. Beltram, and F. Cardarelli, Fast spatiotemporal correlation spectroscopy to determine protein lateral diffusion laws in live cell membranes, Proceedings of the National Academy of Sciences of the

United States of America **110**, 12307 (2013).

[32] W. Thielicke and E. J. Stamhuis, PIVlab – Towards User-friendly, Affordable and Accurate Digital Particle Image Velocimetry in MATLAB, Journal of Open Research Software **2**, 10.5334/jors.bl (2014).